Kent Academic Repository

Liu, Yudong, Zhu, Mingjuan, Wang, Tianxiang, Lei, Gang, Hossain, Md. Moinul, Zhang, Biao, Li, Jian and Xu, Chuanlong (2021) *Spatial resolution of light field sectioning pyrometry for flame temperature measurement.* Optics and Lasers in Engineering, 140 . ISSN 0143-8166.

Downloaded from

https://kar.kent.ac.uk/85621/ The University of Kent's Academic Repository KAR

The version of record is available from

https://doi.org/10.1016/j.optlaseng.2021.106545

This document version

Author's Accepted Manuscript

DOI for this version

Licence for this version

UNSPECIFIED

Additional information

Unmapped bibliographic data:DA - 2021/05/01/ [EPrints field already has value set]JO - Optics and Lasers in Engineering [Field not mapped to EPrints]

Versions of research works

Versions of Record

If this version is the version of record, it is the same as the published version available on the publisher's web site. Cite as the published version.

Author Accepted Manuscripts

If this document is identified as the Author Accepted Manuscript it is the version after peer review but before type setting, copy editing or publisher branding. Cite as Surname, Initial. (Year) 'Title of article'. To be published in *Title of Journal* , Volume and issue numbers [peer-reviewed accepted version]. Available at: DOI or URL (Accessed: date).

Enquiries

If you have questions about this document contact ResearchSupport@kent.ac.uk. Please include the URL of the record in KAR. If you believe that your, or a third party's rights have been compromised through this document please see our Take Down policy (available from https://www.kent.ac.uk/guides/kar-the-kent-academic-repository#policies).

Spatial resolution of light field sectioning pyrometry for flame temperature measurement

Yudong Liu[1,2], Mingjuan Zhu[1], Tianxiang Wang[3], Gang Lei[3], Md. Moinul Hossain[4], Biao Zhang[1], Jian Li[1], Chuanlong Xu[1]*

[1] National Engineering Research Center of Turbo-Generator Vibration, School of Energy and Environment, Southeast University, Nanjing, 210096, China

[2] Huaneng Jiangsu Energy Development Co., Ltd., Nanjing, 210015, China

[3] State Key Laboratory of Technologies in Space Cryogenic Propellants, Beijing, 100028, China

[4] School of Engineering and Digital Arts, University of Kent, Canterbury, Kent, CT2 7NT, UK

Abstract

The light field sectioning pyrometry (LFSP) has proven a significant advancement for in-situ measurement of flame temperature through a single light field camera. However, the spatial resolution of LFSP is limited, which severely inhibits the measurement accuracy. This paper aims to evaluate the spatial resolution of LFSP for flame temperature measurement quantitatively. A theoretical model of the spatial resolution is established based on optical parameters and point spread function of the light field camera. The spatial resolution is then numerically analyzed with different parameters of light field cameras. Based on the theoretical model, a novel cage-typed light field camera with a higher spatial resolution of LFSP is developed and experimentally evaluated. A significant improvement of spatial resolution about 17% and 50% in lateral and depth directions, respectively, is achieved. Results show that the spatial resolution is in good agreement with the theoretical model. The LFSP is then evaluated under different combustion cases and their temperatures are reconstructed.

Keywords: flame temperature measurement, spatial resolution, light field imaging, optical sectioning, 3D reconstruction

1. Introduction

In combustion processes, the flame temperature measurement is essential as it governs the pollutant emissions (NOx), combustion efficiency, and operation safety of furnaces and other combustion devices [1–4]. The in-situ measurement of the three-dimension (3-D) flame temperature with a high spatial resolution is crucial for a better understanding of the combustion processes and design of combustion devices [4–6]. To achieve non-intrusive measurement of the flame, various techniques have been developed based on either the active interaction between the flame and the emitted signal, such as laser-based or acoustic-based techniques [4,6], or the passive flame radiation such as imaging-based techniques [2,3,7–9]. Although the laser-based or acoustic-based techniques usually have higher measurement accuracy, these techniques have a disadvantage of bulky signal emitting and receiving devices. Contrarily, the imaging-based techniques have widely been used for flame temperature measurement due to its ease of implementation and faster responses. The imaging-based techniques usually use a single-camera [2,3] or multiple cameras [8,10] approach to reconstruct the flame temperature through color ratio pyrometry (CRP) technique. However, the single-camera scheme can only retrieve the temperature field of axisymmetric flames due to its limited perspective of flame [3]. The multi-camera scheme can be used for non-symmetric/turbulent flames, which requires multiple cameras to locate around the flame. However, it is difficult to mount the multi-cameras system if the optical access is limited in combustion facilities [4,7,9], such as the gas-turbine combustors and other high-temperature or high-pressure environments [5].

In recent years, the optical sectioning technique (OST) has been proposed to retrieve the 3-D flame temperature field and make it feasible when optical access is limited [11]. The OST reconstructs the 3-D flame temperature as several sections with different depths (i.e., perpendicular to the optical axis of the imaging system) using a stack of photos. Those photos are captured through a single camera from a single direction but focusing on different depth positions. Usually, a mechanical lens or a liquid variable-focus lens is used to focus on different depths of the flame and capture the flame images as a sequence. However, the process of focus adjustment is time-consuming for both the mechanical lens and the liquid variable-focus lens. Although the liquid variable-focus lens adjusts the focus faster, the response time of the focus adjustment is still up to ~40 *ms* to capture a single flame image [12], which makes it difficult to measure the flame temperature instantaneously. Therefore, the OST is unsuitable for the diagnostic of turbulent flames.

To resolve the limit of the focus adjustment time, the light field (LF) imaging technique is proposed. The LF imaging technique can generate photos (known as the LF refocus images) focusing on different depths after a single time exposure of a light field camera (LFC) [13]. By combining the LF imaging with the OST, the light field sectioning pyrometry (LFSP) technique is proposed [14]. The LFSP uses a stack of LF refocus images to reconstruct the sections of flame temperature distribution with different depths along the optical axis of the LFC. Recently, the LFSP technique is used to reconstruct the diffusion flame temperature by not only numerical simulation (while considering the flame as rotationally symmetric) [15], but also experimental study using a commercial LFC [14]. These works demonstrate the feasibility of LFSP for flame temperature reconstruction, but both the number of the reconstructed sections and the size of the flame are different, and thus the spatial resolution of LFSP is not comparable. In fact, the spatial resolution is sacrificed to distinguish the angle of incident light in LF imaging [16], which limits the spatial resolution widely for accurate reconstruction of flame through the LFC. As a result, only 6×6×6 temperature points can be retrieved through the traditional LF-based flame reconstruction method, which reconstructs the flame temperature by solving the ill-posed inverse radiation problem [17]. Later, the spatial resolution of the LFSP in the lateral direction is improved in Ref. [14] and the typical number of grids 100×100×4 is considered to retrieve the flame temperature distribution. However, the spatial resolution of LFSP is limited in the depth direction, and more importantly, it is still unknown that what distances in both the lateral and depth directions can be resolved by the LFSP. Therefore, an effective method is required to evaluate the spatial resolution quantitatively.

A few studies were carried out to improve the spatial resolution of LFSP or other LF imaging applications. For LFSP, the number of sections can be increased by modifying the reconstruction algorithm and mathematical interpolation [15]. However, it is reported that such a modification cannot resolve the limitation of depth resolution by merely increasing the number of sections because it would lead to a strong correlation between the adjacent sections. Consequently, the modified reconstruction algorithm may not be ideal for improving the spatial information and, in some cases, it may increase the computational cost. Therefore, it is necessary to optimize the LFC parameters to obtain adequate spatial information of flame radiation [18]. So that the correlation between the adjacent sections can be reduced, and the depth resolution of LFSP can be improved. Recently, a few studies were proposed to improve the spatial resolution by optimizing the LFC parameters for detecting the depth of opaque objects [19–21]. A relationship between the spatial resolution and the LFC parameters is theoretically derived according to the diameter of the blurry disk while imaging an opaque object [19]. For the particle flow reconstruction, the spatial resolution is analyzed through various reconstruction algorithms [20,22]. However, the flame is fundamentally a translucent and continuous medium in 3-D space, and it is completely different from the opaque objects or particles. Also, the flame radiation is superimposed along the line of sight [4,8]. So, the improvement made by the aforementioned studies is not applicable for the flame reconstruction through the LFSP. Therefore, it is crucial to evaluate the spatial resolution of LFSP quantitatively, also to investigate the potential factors such as imaging characteristics of the LF refocus image, the reconstruction algorithm and LFC parameters. So that the spatial resolution of LFSP can be optimized and the accuracy of flame temperature measurement can be further improved.

This paper aims to evaluate the spatial resolution of LFSP for flame reconstruction. A mathematical relationship is firstly derived among the spatial resolution, LFC parameters, and point spread function of the LFC. The spatial resolution of LFSP is then analyzed numerically under different LFC parameter settings. Subsequently, a cage-typed light field imaging system with optimized parameters is developed with an improved spatial resolution. The developed system is experimentally evaluated under different combustion cases and their flame temperatures are reconstructed. A comparative study is carried out with thermocouple measurements. The instantaneous temperature distribution of a turbulent flame is also reconstructed and discussed.

2. Principle of light field sectioning pyrometry

Fig. 1 illustrates the principle of LFSP, which includes the acquisition of LF raw image of flame, LF refocusing, optical sectioning and color ratio pyrometry (CRP). Firstly, the LF raw image of the flame is acquired by an LFC. Secondly, The LF raw image is then used to generate a stack of LF refocus images at different depths of the flame through a light field refocus algorithm. Thirdly, the stack of LF refocus images is used to reconstruct the spectral radiation distribution of each flame section using an optical sectioning algorithm, which is corresponding to the RGB (red, green, and blue) color channels of an image sensor. Finally, the CRP is used to determine the temperature distribution of each flame section. In this study, the ratio is obtained through red and green channels. The blue channel is ignored due to its low signal-noise-ratio [2].

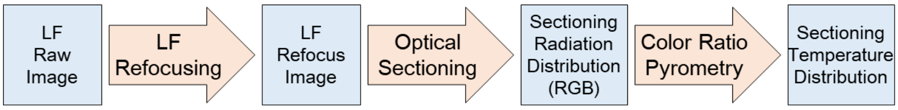

Fig. 1. The strategy of light field sectioning pyrometry technique.

A simplified optical structure and imaging process of an LFC is shown in Fig. 2. The radiation emits from a flame reaches the main lens of the LFC and forms a flame image on the microlens array (MLA). The radiation is then divided by microlenses according to its incident direction and forms sub-images on the CCD (Charge-coupled device) image plane. All those sub-images compose the "honeycomb-shaped" light field raw image and then recorded by the CCD sensor. The light field raw image is decoded as an LF dataset and finally used to generate the images focusing on given depths (i.e., the LF refocus images) [13,23]. To ensure the capability to focus on continuous depths, an LF refocusing algorithm based on the frequency domain is utilized in this study [24,25].

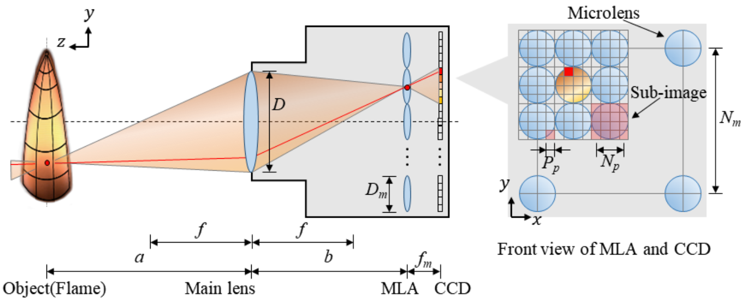

Fig. 2. The fundamental structure of the light field camera (not scaled).

Based on the Fourier optics theory, the optical sectioning process can be described by convolution calculation [26]. The response of an imaging system (e.g., a camera) to a point object can be described using the point spread function (PSF). For a linear space-invariant imaging system, the formed image is the convolution of the object and the PSF, if a planar object is perpendicular to the optical axis of the imaging system [11]. The flame is not a planar object but optically thick, continuous and emitting incoherent radiation [1, 26], which means that the flame radiation intensity emitted from each point of the flame is additive. So, the flame image intensity $E(x,y,\lambda)$ can be calculated by integrating the convolution along the optical axis direction and expressed as:

$$E(x,y,\lambda) = \int f(x,y,z,\lambda) * h(x,y,\mathrm{z})dz \tag{1}$$

where $*$ is the convolution operator, $f(x,y,z,\lambda)$ is the flame radiation intensity distribution, $h(x,y,\mathrm{z})$ is the PSF of the imaging system with the depth positions (z), and λ is the wavelength corresponding to the RGB channels of a camera. If the flame is discretized as a combination of N two-dimensional flame sections (parallel to each other and perpendicular to the optical axis of the imaging system, as shown in Fig. 3), the imaging process can then be discretized as:

$$E(x,y,\lambda) = \sum_{\mathrm{i}=1}^{N} f_i(x,y,\lambda) * h_i(x,y) \tag{2}$$

It is known that the LF imaging system can focus on only one depth (i.e., corresponding to one section) sharply at a time. The rest of the sections are defocused and blurred. Therefore, the defocused flame sections would make a significant contribution to the image intensity. As the flame is translucent, it is more challenging to remove the intensity contribution of the defocused flame section and reconstruct the intensity contribution of the focused section accurately.

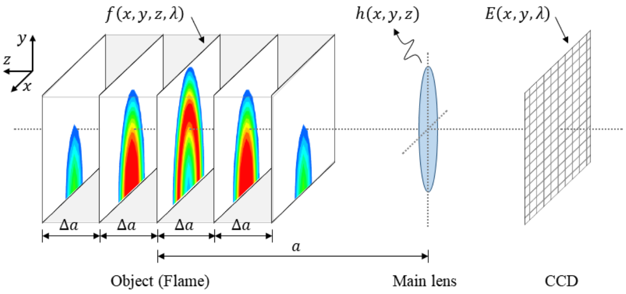

Fig. 3. Schematic of the optical sectioning reconstruction of a flame (not scaled).

To improve the reconstruction accuracy, the Van Cittert algorithm is used because it can reconstruct the flame sections by minimizing the sum of the squared error between the recorded and the estimated image from the reconstructed sections [27]. As an iterative deconvolution method with the non-negativity constraint, the Van Cittert algorithm has successfully been used for the flame reconstruction through LFSP [14]. To perform the Van Cittert algorithm, it is required to set various depth positions of multiple reconstructable sections (referring to Fig. 3) manually. The LF refocus images obtained from these manual-setting depth positions are then used to estimate the flame sections with the knowledge of the PSFs of the optical system. After a few iterations, the intensity contribution of the defocused flame sections can be removed and multiple sections corresponding to those manual-setting depth positions can be reconstructed simultaneously [11]. It should be noted that the manual-setting depth positions of the sections should be determined carefully because it would impact the accuracy of the deconvolution calculation [14], which is described in Section 3.2.

Once the flame radiation intensity [i.e., $f_i(x,y,\lambda)$ in Eq. (2)] are reconstructed under different depths, the CRP technique is then used to reconstruct the temperature distribution. The CRP mainly measures the temperature of the soot particles [2]. For diffusion flames, the radiation is the thermal radiation emitting from the soot. To eliminate the effect of soot concentration, the CRP uses the ratio of spectral radiation intensity to calculate the flame temperature [2, 28]. For RGB images, the CRP can be expressed as:

$$T = g(R/G) \tag{3}$$

where T is temperature, R and G are the radiation intensity of the red and green channels, g is the function between T and R/G, which is calibrated through the experiment, as discussed in Section 5.4. The detailed implementation and verification of the CRP technique can be found elsewhere in [29].

3. Spatial resolution of LFSP

3.1 Point spread function

The PSF [i.e., $h_i(x,y)$ in Eq. (2)] has a significant effect on the flame reconstruction accuracy and the spatial resolution of the LFSP. The PSF is referred to the LF refocus image of a point, which means that the PSF depends on the LFC parameters, the refocusing depth position and the position of the object plane (i.e., a in Fig. 2). Therefore, it is desirable to establish a relationship between the spatial resolution and the LFC parameters through PSF. To achieve that, the PSF is modeled as a 2D Gaussian distribution [14,30] which is given as:

$$h_G(x,y) = \frac{1}{\pi\sigma^2} \cdot \exp\left(-\frac{x^2+y^2}{2\sigma^2}\right) \tag{4}$$

where σ is the standard deviation of the Gaussian distribution, the x and y are the pixel position on the PSF image according to the coordinate system, as shown in Fig. 3. In the Gaussian PSF model, the diameter of the PSF is determined using the full width at half maximum (FWHM) [31], which is given as:

$$FWHM[h_G(x,y)] = 2\sqrt{2ln2} \cdot \sigma \tag{5}$$

Since the PSF image is a spatially discrete digital image, the actual diameter of the PSF (ϕ_{PSF}) can be solved as:

$$\phi_{PSF} = FWHM[h_G(x,y)] \cdot \Delta_p \tag{6}$$

where Δ_p is the pixel size of the PSF image. For the LF refocus image of a point on an LFC, the pixel size is equal to the diameter of the microlens, i.e., $\Delta_p = D_m$. Therefore, the actual diameter of the PSF can be solved if D_m and σ are known. The value of σ can be determined through calibrations, as discussed in Section 5.3.

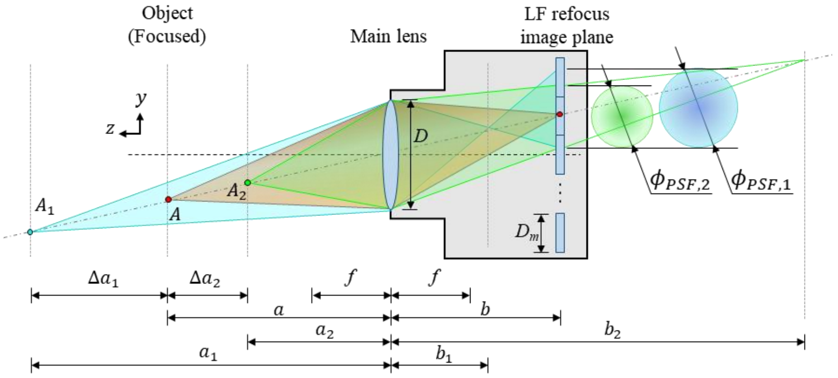

Fig. 4. Schematic of the PSF with depth positions of the objects. The LF refocus image is focused on the object point *A*. The object points *A₁*, and *A₂* are defocused and forming circular PSF spots. The imaging system is simplified as a conventional camera, where the LF refocus image is the discrete according to the MLA of LFC.

From an optical point of view, the actual diameter of the PSF is related to the LFC parameters and the depth position of the object point. If an object point is focused (i.e., located on the object plane), the image of it is an infinitesimal point on the image plane. But if the object point is defocused and away from the object plane, it forms a circular PSF spot, instead. Fig. 4 shows a schematic of the circular PSF when the object is defocused (A_1 and A_2) or focused (A) on the LF refocus image plane. In Fig. 4, the focal length of the main lens is f, the object distance is a, the distance between the main lens and the LF refocus image plane is b, and the diameter of the main lens aperture is D. The points A, A_1, and A_2 are the object points, where the subscripts 1, 2 indicate that the object point is far from or close to the imaging system, respectively. a_i $(i = 1,2)$ is the distance between the defocused object and the main lens. Δa is the defocused distance between the object plane and the object point, i.e., $\Delta a = a_i - a$. $\Delta a > 0$ means the object is far away from the imaging system and vice versa. While the LFC parameters and the defocused distance are given, the actual diameter of the PSF image spot (ϕ_{PSF}) can be solved based on the Gaussian lens formula and the geometric similarity [26],

$$\phi_{PSF} = \frac{|\Delta a| \cdot f \cdot D}{(a+\Delta a) \cdot (a-f)} \qquad (\Delta a > f - a) \tag{7}$$

where the condition $\Delta a > f - a$ is to form a real image. Note that Eq. (7) is not applicable if the object is precisely on the object plane ($\Delta a = 0$), in which the ϕ_{PSF} is governed by the diffraction limit (discussed in Section 3.3). By combining Eqs. (6) and (7), σ is closely relevant to the LFC parameters and the defocused distance.

3.2 Depth resolution of LFSP

The depth resolution of LFSP is defined as the space between the adjacent flame sections. As discussed in Section 2, such a space is governed by the manual-setting depth positions in the optical sectioning process. It seems that the depth resolution can be improved if the depth positions of the sections are set close to each other. However, the depth positions of the flame section affect the flame reconstruction accuracy significantly [14]. If the depth positions of the flame sections are set closer to each other (i.e., the smaller space between the sections), the similarity of the images (focusing on these depth positions) will be increased because their corresponding PSFs can be similar to each other. Subsequently, these similarities create further difficulty in removing the intensity contribution of the defocused flame sections and thus affect the reconstruction accuracy. Therefore, ensuring the reconstruction accuracy of LFSP is a crucial prerequisite to improve spatial resolution. For example, while reconstructing the focused flame section (i.e., on the object plane), the defocused distance Δa [refer to Eq. (7)] of the adjacent section can be set as small as possible where the reconstruction accuracy is ensured. Hence, the depth resolution can be considered by solving the defocused distance (Δa) of the defocused section for the accurate reconstruction. If the defocused section is far from the imaging system ($\Delta a > 0$) the defocused distance Δa_1 can be solved as:

$$\Delta a_1 = \frac{a \cdot \phi_{PSF,DR} \cdot (a-f)}{f \cdot D - \phi_{PSF,DR} \cdot (a-f)} \tag{8}$$

where the $\phi_{PSF,DR}$ is the actual diameter of the PSF of the adjacent defocused sections when the reconstruction is accurate. If the distance between the defocused flame section and the focused flame section is larger than Δa_1, the contribution of the defocused flame sections can be removed accurately. According to Eq. (7), the range of $\phi_{PSF,DR}$ is $\left(0, \frac{f \cdot D}{a-f}\right)$. In the case that the defocused section is close to the imaging system, the defocused distance Δa_2 is given as:

$$\Delta a_2 = \frac{a \cdot \phi_{PSF,DR} \cdot (a-f)}{-f \cdot D - \phi_{PSF,DR} \cdot (a-f)} \tag{9}$$

where $\phi_{PSF,DR} \in (0, D)$. For the LFSP, the reconstructed flame section is accurate if the interval between the defocused flame sections and the focused flame section is larger than the limit of Δa_1 and Δa_2 on both sides of the focused flame section. Therefore, the depth resolution (DR) is given as the interval between the defocused sections on both side, which is expressed as:

$$DR = \Delta a_1 - \Delta a_2 = \frac{a \cdot \phi_{PSF,DR} \cdot (a-f)}{f \cdot D - \phi_{PSF,DR} \cdot (a-f)} + \frac{a \cdot \phi_{PSF,DR} \cdot (a-f)}{f \cdot D + \phi_{PSF,DR} \cdot (a-f)} \tag{10}$$

A smaller DR means that the smaller depth distance can be resolved, and more spatial detail can be reconstructed along the depth direction. Note that Eq. (10) is similar to the depth-of-field formula for a conventional camera [26], but the physical meaning and value of $\phi_{PSF,DR}$ here are different. The calculation of the depth of field for a conventional camera typically uses the circle of confusion diameter, referring to the size of a pixel. But the determination of $\phi_{PSF,DR}$ is important including the reconstruction algorithm and the characteristics of flame radiation transmission. In this study. the value of $\phi_{PSF,DR}$ can be solved through numerical simulation, as discussed in Section 4.

3.3 Lateral resolution of LFSP

The lateral resolution refers to the minimum separation on a flame section, which can be resolved by the LFSP. As discussed in Section 2, the discretization of the 3-D object space is determined in the process of the LF refocusing. According to the LF refocus technique, the number of pixels along the x or y direction of the reconstructed flame section is the same as that of the LF refocus image, which is equal to the number of microlenses on the MLA [13]. Therefore, each microlens corresponds to an area on the object plane [20]. According to the geometric optics, the length of the area on the object plane is D_m/M, where M is the magnification of the LF refocus image and $M = f/(a-f)$. The lateral resolution (LR_{PSF}) can be defined as:

$$LR_{PSF} = FWHM[(D_m/M) * h_G(x,y)] \tag{11}$$

where $*$ is the convolution operator.

According to the wave optics, the light from a best-focused spot forms a diffraction pattern rather than an infinitesimal point, even if the aberrations of the main lens is negligible. In the center of the diffraction pattern, the brightest circle bounded by a dark ring is known as the Airy spot. Based on the Fraunhofer diffraction of the circular aperture [26], the radius of the Airy spot R_{Airy} is given by $R_{Airy} = 1.22 f\lambda/D$, where λ is the wavelength of light. The diameter of the Airy spot represents the limit of lateral resolution that the imaging system can distinguish due to the diffraction restrictions. The lateral resolution limited by the Airy spot is given as:

$$LR_{\mathrm{Airy}} = 2 \cdot R_{Airy}/M \tag{12}$$

Hence, the overall lateral resolution is governed by the larger one between LR_{PSF} and LR_{Airy}, so the lateral resolution (LR) of the system is expressed as:

$$LR = Max\{LR_{PSF}, LR_{Airy}\} \tag{13}$$

A smaller LR means that the smaller lateral distance can be resolved, and more detail on a flame section can be reconstructed.

4. Numerical analysis of the spatial resolution

4.1 Simulation setup

It is crucial to obtain the $\phi_{PSF,DR}$ [refer to Eq. (10)] value to investigate the spatial resolution of LFSP. The value of $\phi_{PSF,DR}$ depends on the LFC parameters and the PSF parameter σ [Eq. (6)]. Therefore, the value of $\phi_{PSF,DR}$ can be determined if the σ of the adjacent defocused section is solved. In this study, the σ of the adjacent defocused section is denoted as $\sigma_{neighbor}$. To determine the value of $\sigma_{neighbor}$, numerical simulation is carried out to reconstruct the temperature distribution of a flame. A cylindrical flame model is considered in this study to determine the value of $\sigma_{neighbor}$ and the model is expressed as:

$$T(x,y,z) = t_1 \cdot \exp\left\{-\left[m\left(\frac{z^2}{Z^2} + \frac{x^2+y^2}{R^2}\right) - n\right]^2\right\} + t_2 \quad (K) \tag{14}$$

where x, y, and z are coordinate values, as explained in the coordinate system in Fig. 2. The origin is at the bottom center of the flame. $t_1 + t_2$ is the maximum temperature, t_2 is the minimum temperature, m is the gradient of temperature, n is the normalized position of the highest temperature, Z and R are the height and radius of the flame, respectively. The flame temperature considered in this study are $t_1 = 1200\,K$, $t_2 = 900\,K$, $m = 10\,K$, $n = 0.4$, $Z = 75\,mm$, $R = 25\,mm$, as shown in Fig. 5. According to Planck's law, the spectral radiation intensity I_λ of the soot particles can be determined as:

$$I_\lambda = \frac{c_1 \lambda^{-5}}{\exp\left(\frac{c_2}{\lambda T}\right)-1} \cdot \frac{\varepsilon}{d\Omega \cdot \cos\theta} \quad (15)$$

where T is temperature, λ is the wavelength, c_1 and c_2 are the first and second radiation constant, ε is the emissivity of the soot particles, Ω is the solid angle (sr), and θ is the zenith angle of the emitted radiation. The wavelength considered in this simulation is $\lambda = 633nm$. The unit of the spectral radiation intensity I_λ is $W \cdot m^{-3} \cdot sr^{-3}$. As soot particles emit in the 3-D space, the solid angle is considered as $d\Omega \cdot \cos\theta \approx 4\pi$. Once the radiation starts propagating, the absorption and scattering of the flame would affect the radiation intensity until the radiation reaches the surface of the flame. According to Beer-Lambert law [32], when the radiation reaches the surface of the flame, the spectral radiation intensity $I_{\lambda,L}$ is given as:

$$I_{\lambda,L} = I_{\lambda,0} \cdot \exp(-\beta_\lambda L) \quad (16)$$

where $I_{\lambda,0}$ is the spectral radiation intensity when the radiation is emitted, L is the length of the path that the beam of radiation propagating through the flame medium, which can be solved by ray-tracing technique [18]. The attenuation coefficient β_λ is given by $\beta_\lambda = \kappa_{a,\lambda} + \sigma_{s,\lambda}$, where $\kappa_{a,\lambda}$ and $\sigma_{s,\lambda}$ are the absorption coefficient and the scattering coefficient, respectively. In this study, the absorption coefficient $\kappa_{a,\lambda} = 8\,m^{-1}$ is considered according to the property of ethylene diffusion flame [3,7]. The effect of scattering is ignored because it is much smaller than the effect of absorption for a flame [33]. This simplification is proved by the Mie theory [34]. The obtained $I_{\lambda,L}$ values from the entire flame are subsequently used in the image generating process.

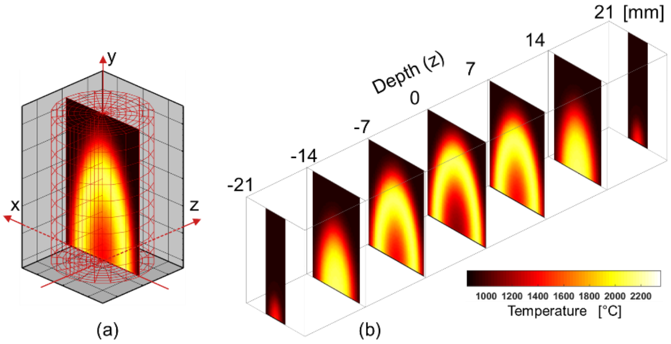

Fig. 5. (a) An axisymmetric cylinder flame model and (b) sectional flame temperature distributions at different depths.

To simplify the image generating process, the LF refocus image is achieved through the convolution of the PSF and the contribution of the radiation intensity of each flame section [refer to Eq. (2)]. Such a simplification is based on the fact that if the image is discretized in the same number of pixels, the LF refocus image is equivalent to the image directly recorded by a conventional camera [14]. While applying Eq. (2) the number of flame sections is $N = 400$ to reduce the errors caused by image dispersion in the image generating process. The PSF of the focused section is fixed as $\sigma = 1$. The PSF of the defocused section adjacent to the focused section varies in the range of $\sigma_{neighbor} \in (1,4)$. A larger $\sigma_{neighbor}$ means that the adjacent section is blurred significantly. The PSF of other sections can be solved using the Eqs. (6) and (7) and the linear interpolation.

4.2 Relationship between the reconstruct accuracy and the PSF

To investigate the relationship between the reconstruction accuracy and the PSF, the flame section at $z = 0$ *mm* is considered to reconstruct through the LFSP. Fig. 6 shows the examples of the original and reconstructed flame sections at $z = 0$ *mm* under different $\sigma_{neighbor}$ values and iterations. In Fig. 6(a), it can be seen that the flame temperature is relatively lower in the center and the higher in the edge of the flame (bright yellow area). The reconstructed results achieved under different $\sigma_{neighbor}$ and iterations are presented in Figs. 6(b)-6(d). When $\sigma_{neighbor}$ = 1.2 and iterations = 10, the reconstructed temperature distribution is uniform and significantly inaccurate compared to the original. However, the reconstructed temperature distribution is like the original while increasing the $\sigma_{neighbor}$ and iteration. Therefore, it is evident that larger $\sigma_{neighbor}$ and iteration provides better reconstruction accuracy.

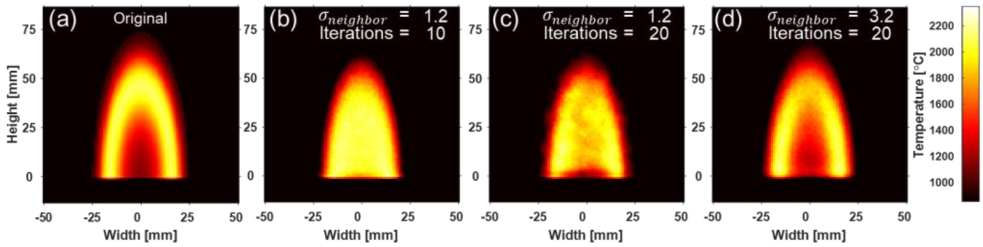

Fig. 6. Original temperature distribution at z = 0 *mm* (a), reconstructed temperature distribution at (b) $\sigma_{neighbor}$= 1.2 and iterations = 10, (c) $\sigma_{neighbor}$=1.2 and iterations = 20, and (d) $\sigma_{neighbor}$ = 3.2 and iterations = 20.

To further evaluate the reconstruction accuracy, the structural similarity index (SSIM) is used to compare the reconstructed center flame section (i.e., $z = 0\ mm$) with the ground truth[35]. The SSIM provides the similarity between these two distributions based on brightness, structure and contrast [36], which is defined as:

$$SSIM(x,y) = l(x,y)^{\alpha} \cdot c(x,y)^{\beta} \cdot s(x,y)^{\gamma} \tag{17}$$

where *x* and *y* refer to the original and the reconstructed flame section, respectively. The term of $l(x,y)$, $c(x,y)$, and $s(x,y)$ refers to the difference of brightness, structure and contrast, where the indices are set as $\alpha = \beta = \gamma = 1$. The value of SSIM is between 0 and 1. A larger SSIM value presents higher reconstruction accuracy.

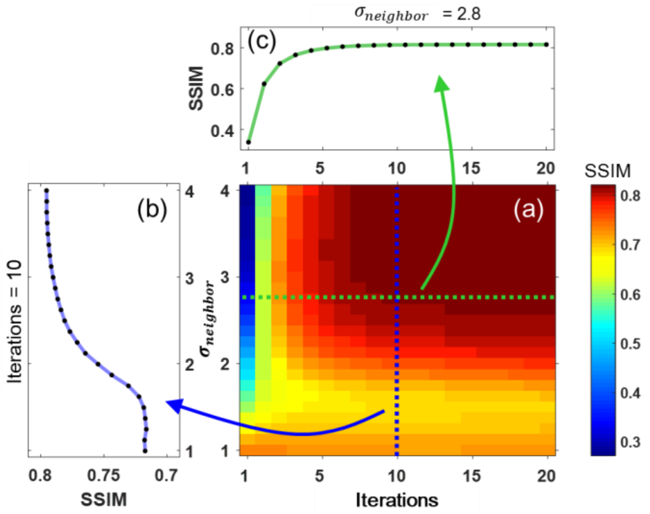

Fig. 7. The bi-variate distribution of SSIM of the reconstruction results with $\sigma_{neighbor}$ and iterations (a), the SSIM with $\sigma_{neighbor}$ at 10 iterations (b), and the SSIM with iterations when $\sigma_{neighbor}$ = 2.8(c).

The bi-variate distribution of SSIM with different $\sigma_{neighbor}$ and iterations is shown in Fig. 7. From Fig. 7(a), it can be seen that the SSIM increases with the increase of both $\sigma_{neighbor}$ and iterations. This result is consistent with the reconstructed distribution, as shown in Fig. 6. It is also observed that no matter how the $\sigma_{neighbor}$ and the iterations are increased, there is no further increment for SSIM after $\mathrm{SSIM} \approx 0.8$, as shown in Fig. 7(a). With fixed iteration and increment of $\sigma_{neighbor}$, SSIM firstly remains low and then significantly increases at $\sigma_{neighbor} > 1.5$. Fig. 7(c) illustrates that when $\sigma_{neighbor}$ is fixed, the SSIM increases rapidly with the increase of iteration, and subsequently, the SSIM almost stops increasing when the iteration is more than ten. Besides, Fig. 7(a) illustrates that the SSIM remains low no matter how many iterations are processed if $\sigma_{neighbor} < 2$. On the other hand, there are costs to increase either $\sigma_{neighbor}$ or the iterations. For example, a larger $\sigma_{neighbor}$ requires a larger defocused distance or the changing of the LFC parameter, whereas a larger number of iterations increases the computation cost. Thus, the smallest $\sigma_{neighbor}$ and the iterations should be chosen if the SSIM is not increased. As a tradeoff, $\sigma_{neighbor} = 2.8$ and ten iterations are considered in this study to reconstruct the flame temperature accurately through the LFSP.

4.3 Spatial resolution

Once the optimum value of $\sigma_{neighbor}$ is determined, the depth and lateral resolution of LFSP can be obtained using Eqs. (10) and (13). Fig. 8 illustrates the depth resolution of LFSP. The standard deviations of the PSF (σ) with the defocused distances (Δa) are calculated through Eqs. (6) and (7) and the proposed cage-typed LFC (discussed in Section 5) parameters illustrated in Table 1. The σ increases when Δa increases from zero to positive or negative directions. Note that the range of Δa is $\Delta a \in \left(f-a,+\infty\right)$ according to Eq. (7). If Δa increase to both ends of its range, the σ will reach its local maximums, which are given as:

$$\begin{cases} \sigma_f = \lim\limits_{\Delta a \to f-a} \sigma = \frac{D}{2\sqrt{2ln2}\cdot D_m} \\ \sigma_{+\infty} = \lim\limits_{\Delta a \to +\infty} \sigma = \frac{fD}{2\sqrt{2ln2}\cdot D_m\cdot(a-f)} \end{cases} \tag{18}$$

The optimum value of $\sigma_{neighbor} = 2.8$ is denoted as a horizontal red dash line in Fig. 8. Two cross points (green points in Fig. 8) are formed between the red dash line and the distribution of σ. The interval between these two cross points is the depth resolution obtained through the proposed cage-typed LFC parameters.

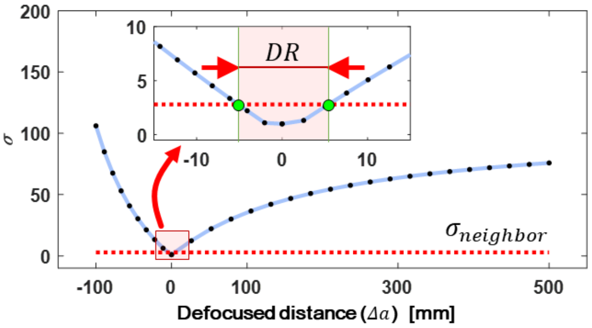

Fig. 8. The standard deviation of the PSF (σ) with the defocused distance Δa.

A comparative study was carried out to investigate the depth and lateral resolution of different LFC parameters. The different LFC parameters and their depth and lateral resolution are shown in Table 1. It can be seen that the depth resolution (DR) varies significantly with the LFCs. The depth resolution of the Raytrix R29 [18] is 2027.04 mm, which is worsened than the other LFCs. The maximum σ of PSF for the Raytrix R29 is solved as $\sigma_f = 32.17$ and $\sigma_{+\infty} = 3.58$. The requirement of $\sigma_{neighbor}$ is close to $\sigma_{+\infty}$, which increases the defocused distance significantly in the further side (Δa_1) and increases the DR. Note that if $\sigma_{neighbor}$ is larger than $\sigma_{+\infty}$, the intensity contribution from the defocused flame sections would be difficult to remove completely, which makes the DR infinite. This effect is known as hyper-focal distance [37]. In addition, it is worth to note that the DR of Raytrix R29 is larger than the spatial resolution in related studies [14,17]. This is because the spatial resolutions in references [14] and [17] represent the size of the grid, which is determined manually to achieve the reconstruction effectively. However, although a denser grid improves the spatial resolution, the accuracy of reconstruction will be significantly reduced. In this work, the DR reveals the smallest grid size when the reconstruction accuracy is guaranteed. It can also be seen that the DR of the proposed cage-typed LFC is reduced to 50% compared to the best of Lytro Illum LFC.

Table 1. The parameters of typical LFCs and their spatial resolution of LFSP [unit: mm]

Parameter	**Symbol**	**Raytrix R29**[18]	**Ng Ren**[13]	**Lytro Illum** [37]	**Cage-LFC (Proposed)**
The diameter of the microlens	D_m	0.165	0.125	0.020	0.100
Object distance	a	500	500	150	200

The focal length of the main lens	f	50	140	22	100
The diameter of the main lens	D	12.5	35	11	25
LFSP lateral resolution	LR	1.45	0.32	0.12	0.10
LFSP depth resolution	DR	2027.04	60.78	21.03	10.56

The lateral resolution (LR) of the LFCs is calculated based on Eq. (13). The LR of the proposed cage-typed LFC is 17% smaller than the Lytro Illum. Besides, it is observed that the LR is generally better than DR in all LFCs listed in Table 1. The DR is 100 times larger than the LR and this significant difference can be explained by the characteristics of the light field imaging. As discussed in Section 2, the LR of LFSP should be the same as the lateral resolution of the LF refocus image, which is physically determined by the number of microlenses. Whereas, the DR is determined based on the PSF ($\sigma_{neighbor}$) and the LFC parameters (i.e., the focal length of the main lens, the object distance the diameter of the main lens aperture, the diameter of the microlens) referring to Eqs. (5), (6) and (10). The $\sigma_{neighbor}$ is always larger than the σ of the focused image, that is, $\sigma_{neighbor} > 1$, as shown in Fig. 8. Therefore, it can be concluded that the depth and lateral resolution can be increased or decreased at the same time. However, the depth resolution would not exceed the lateral resolution, no matter how the LFC parameters are optimized.

5. Proposed cage-typed light field camera

5.1 The cage-typed light field camera

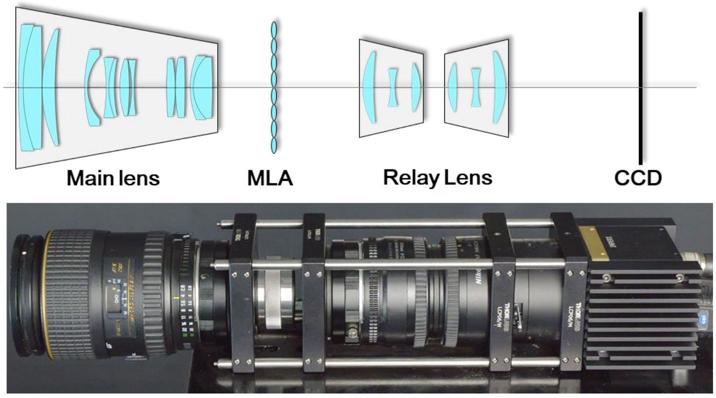

Fig. 9. The structure of the proposed cage-typed LFC.

In this study, a cage-typed light field camera is developed and implemented as a proof of concept to perform the LF imaging. The cage-typed LFC contains the main lens, the MLA, the relay lens, and the CCD sensor, as shown in Fig. 9. All the components are fixed on the cage plates, respectively. The cage plates are then connected by four stainless steel rods. The relay lens is used to ease the assembling of MLA[38,39]. The relay lens consists of two head-to-head Nikon NIKKOR 50 *mm f/1.8*D lenses and is arranged as an optically symmetrical structure to eliminate the imaging chromatic aberration. This arrangement is crucial to improve the reconstruction accuracy in the CRP process. The vignetting caused by the relay lens can be minimized by setting the apertures of the two relay lenses differently. The MLA-side lens is set as *f/1.8* to receive the maximum luminous flux, and the CCD-side lens is set as *f/8* to reduce the vignetting and aberrations [40]. The fundamental parameters of the cage-typed LFC are shown in Table 2. The camera model is Imperx B3340 with the CCD of KAI-08050, and the number of the pixel is 3296 (H) × 2472 (V). To further reduce the vignetting, the edge area of the captured image is cropped, and the cropped image used in the following process is 1850 × 1850. The cage-typed LFC is set as the standard LFC model according to the prototype of Ng [13]. It offers several advantages in comparison to commercial LFC such as (a) the optical components can easily be replaced for various scenarios, (b) all the components (i.e., the main lens, the MLA, the relay lens, and the CCD sensor) of the imaging system share the same optical axis so that the assembling error is minimized, and (c) the position of each optical component can be adjusted accurately.

Table 2. The parameters of the cage-typed LFC

Parameter	Symbol	Value	Unit
Object distance	a	200	mm
The focal length of the main lens	f	100	mm
The diameter of the main lens	D	25	mm
The focal length of the microlens	f_m	420	μm
The diameter of the microlens	D_m	100	μm
The pixel size	p_p	5.5	μm

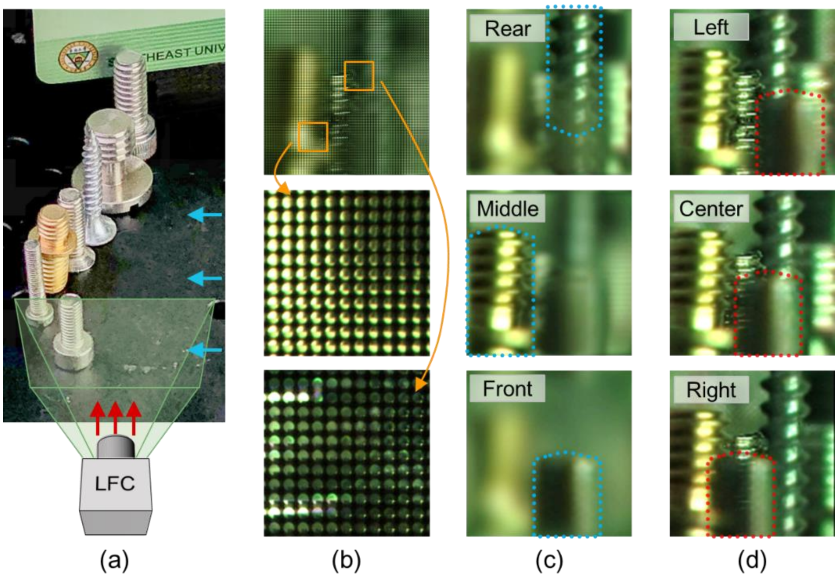

Fig. 10. (a) A sample of LF imaging. The scene of LF imaging, (b)the LF raw images, (c) the LF refocus images (see **Video 1**), and (d) the LF view-shift images of screws (see **Video 2**). The orange frame marks the close-up area showing below the LF raw image. The blue arrows are the LF refocusing depth positions, and the red arrows are the LF view-shifting perspective viewpoints.

To verify the assembled cage-typed LFC system, an experiment was carried out and collected the LF data. A scene with solid objects is used in this experiment, as shown in Fig. 10. The scene contains several screws located from near to far. The captured LF raw images are shown in Fig. 10(b), in which two close-up images are shown as marked with orange frames. The LF raw image consists of an array of round-shaped sub-images. The LF refocus images are also shown in Fig. 10(c). When refocusing at different depth positions, the screws become clear or blurred based on the depth positions. In the figure, the blue dashed lines marked the focused screws in each LF refocused image. The depth positions of the corresponding LF refocus images are marked as blue arrows in Fig. 10(a). Fig. 10(d) shows a set of LF view-shift images generated from the LF raw image by shifting the perspective viewpoint from left to right within the range of the main lens aperture [13]. The depth of field for LF view-shift images are extended and makes that all the objects in different depths are barely blurred. The perspective viewpoints of the LF view-shift images are marked as red arrows in Fig. 10(a). In Fig. 10(d), it can be seen that, when the perspective view is shifted, the foreground (marked with red dashed lines) and background objects moved in opposite directions, and the focused objects are almost static. Similar cases are illustrated in Ref. [23,37,40,41] and consistent with the theory of light field imaging [13]. It demonstrates that the cage-typed LFC system is assembled precisely. To further evaluate the cage-typed LFC system, various calibrations were carried out to utilize the proposed cage-typed LFC system for LFSP. The calibrations include (a) LF refocused depth position, (b) PSF of LFC, and (c) temperature calibration through a blackbody. The detailed descriptions of each calibration can be found in the following sections.

5.2 LF refocus depth position

In the LFSP calculation, the refocused depth position of the LF refocus image should be set accurately for the corresponding flame sections. The refocus depth position (d) can be determined by the parameter of refocusing slope (s) [23,25]. However, the mathematical relationship between d and s are unsolvable because the optical structure of the main lens is unknown. Therefore, it is needed to establish a relationship between the d and s through a calibration. The calibration was carried out by using a calibration plate with black and white checkerboard pattern [14]. The plate is placed perpendicular to the optical axis of the LFC. The object distance from this plate to the front edge of the LFC is measured accurately. The cage-typed LFC is used to capture an LF raw image of the calibration plate. A stack of LF refocus images are then obtained by traversing the refocusing parameters (s). It is required to obtain one of the sharpest LF refocus image on the plate. The sharpest LF refocus image is determined by evaluating all the LF refocus images through image sharpness evaluation function [11,42]. Subsequently, the refocusing parameter (s) corresponding to the sharpest image is linked with the measured object distance. Besides, $d = 0\,mm$ is defined as the object distance when the image of $s = 0$ is the sharpest, in this case, the calibration plate is 110 mm away from the camera lens. By changing the object distance of the calibration plate and repeating the aforementioned processes, the relationship between the refocusing parameter (s) and the refocus depth position (d) can be obtained as $d = f(s)$. Fig. 11 shows the relationship between the s and the d and the fitting function. The coefficient R^2 between the experimental data and the fitting function is 0.9984, which means the fitting function can be used to predict the refocused depth position of the LF refocus image accurately.

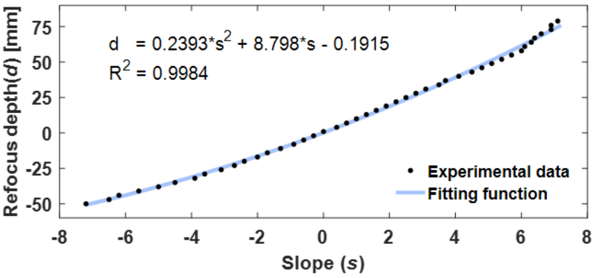

Fig. 11. The LF refocus depth position with the refocus parameter.

5.3 Estimation of PSF of the LFC

As discussed in Section 3.1, the parameter σ is a crucial factor to characterize the PSF of the proposed LFC. To solve the value of σ, a calibration was carried out based on the edge method [43]. Since the PSF is rotationally symmetric [18], the PSF model of Eq. (3) can be integrated along a line to obtain the line spread function (LSF). The LSF is expressed as:

$$l(x) = \int_{-\infty}^{+\infty} h(x,y)dy = \frac{1}{\sqrt{\pi}\sigma}\exp\left(-\frac{x^2}{\sigma^2}\right) \tag{19}$$

A calibration plate with a black and white sharp edge is used to capture a straight boundary using the LFC. The σ in Eq. (19) can then be revealed by analyzing the intensity variation of the black and white boundary in the LF refocus images, as shown in Fig. 12(a). The image intensity variation of the black and white boundary is achieved by the edge spread function (ESF), which is given as:

$$e(x) = \frac{1}{2}erf\left(\frac{x}{\sigma}\right) + \frac{1}{2} \tag{20}$$

where $\operatorname{erf}(x) = \frac{2}{\sqrt{\pi}}\int_{-\infty}^{x}\exp(-t^2)dt$ is the error function. The σ is then solved by fitting the image intensity variation of the corresponding black and white boundary image. Note that the process of LF refocusing is like the change of the focusing depth position of the conventional camera via focus adjustment. In other words, refocusing on a given depth means that an imaging system is formed with specific optical parameters. When two LF refocused images are focusing on different depths, their corresponding PSFs would be different, and these PSFs should be calibrated separately. Therefore, a series of LF refocus images of the calibration plate are obtained by traversing the plate depth position (z) and the refocus depth position (d) separately. Finally, The PSFs with the object depth position (z) and the refocus depth position (d) can be determined by solving the σ corresponding to each image and expressed as $\sigma = g(z, d)$. The 2D distribution of PSF with object depth and refocus depth position obtained by calibration are shown in Fig. 12(c).

To verify the theoretical model of the PSF (discussed in Section 3.1), a comparative study was carried out between the theoretical and experimental values of the PSF with different object depth positions (z) when focusing on the object plane $(d = 0\ mm)$. Note that the defocused distances in Eq. (7) can be solved as $\Delta a = z - d$. The comparative results are shown in Fig. 12(b). A good agreement between the theoretical prediction and the experimental results can be seen, which means that the proposed PSF model is accurate. Thus, the depth resolution predicted by numerical simulation is also correct.

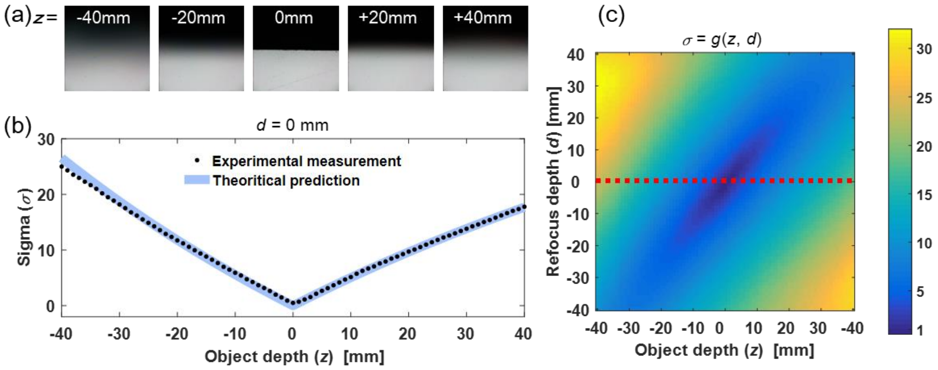

Fig. 12. Examples of LF refocus image of the black and white boundary with object depth positions while refocusing on $d = 0\ mm$ (a), the PSF with object depth positions while refocusing on $d = 0\ mm$ (b), the 2D distribution of PSF with object depth position and refocus depth position (c).

5.4 Temperature calibration through a blackbody

Temperature calibration was carried out to establish a relationship between the temperature and the color ratio (CR) of the flame spectral radiation captured by the CCD sensor [29]. A pre-calibrated blackbody furnace (Land R1500T) is used as the standard instrument for temperature calibration. The blackbody furnace emits thermal radiation with known emissivity (0.999) at an accurate temperature (±1°C at 800-1500°C). The experiment setup is shown in Fig. 13(a), and examples of the obtained LF refocus images are shown in Fig. 13(b). The color ratio is determined using $CR = \overline{R}/\overline{G}$, where the $\overline{R}$ and $\overline{G}$ are the summation of the image pixel intensity of red and green channels, respectively. The CR with temperatures of each LF refocus image and the obtained fitting function are shown in Fig. 13(c). The images used for calibration contains 60 LF refocus images of the blackbody. To evaluate the calibration accuracy, the fitting function is then used to solve the temperature of another 20 LF refocus images of the blackbody. The comparison between the measured temperature and the true temperature of the blackbody is shown in Fig. 13(d). The maximum error is 40.5°C at 1450°C. It demonstrates that the temperature calibration of LFSP is reliable. The obtained fitting function can be used to calculate the flame temperature accurately.

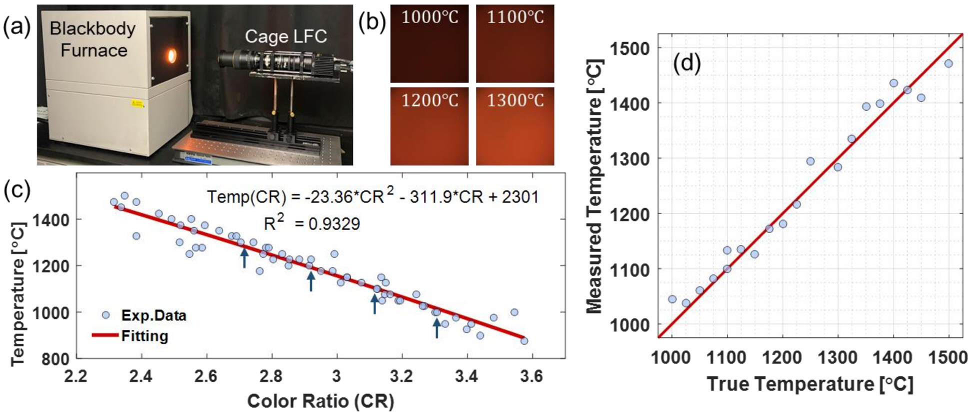

Fig. 13. Temperature calibration setup (a), example LF refocus images of the blackbody furnace with temperature (b), the relationship between the blackbody temperature and the color ratio of the LF refocus images (c), comparison between the measure and true temperature of the blackbody (d). The blue arrows denote the blue dots corresponding to the four example images of the blackbody furnace.

6. Experimental results and discussion

6.1 Experiment setup

To evaluate the proposed LFSP technique, experiments were carried out to generate ethylene-air laminar, double peak and turbulent diffusion flames under different operation conditions. Fig. 14 shows the schematic diagram of the experimental setup. The LFC is mounted on the optical platform through a height-adjustable laboratory jack. During the LF raw image acquisition, the ambient light is blocked by a dark chamber to reduce its impacts. The burner is fixed directly on an optical platform. A replaceable nozzle plate is fixed in the center of the burner, shown as the red circle in Fig. 14. The ethylene (C_2H_4) fuel is injected from the nozzle/nozzles on the pre-designed nozzle plate. The annular air nozzle surrounds the nozzle plate. When air is injected through the annular nozzle, a circular air curtain is formed to provide the oxidizer and to protect the flame from surrounding room air movements [17]. The annular air nozzle has an insert of glass bead (diameter 3 *mm*) and meshes to minimize the flow non-uniformity. The flow rate of ethylene and air are controlled by two mass flow-meters (Sevenstar CS200A), separately. Note that the replaceable nozzle plates are used to adjust the number, layout, and diameter of the nozzle so that various flames can be generated.

Three different nozzle plates, as shown in Fig. 14, were used in this study to create three different combustion cases and to achieve three different structures of flames, i.e., the laminar, double-peak, and turbulent flames. Those three flames are measured in three separate experiments for various purposes. The first experiment (i.e., laminar diffusion flame experiment) is carried out to verify the reconstruction accuracy of flame temperature through the LFSP because it is stable and has a high gradient temperature distribution. A nozzle plate with one fuel nozzle is used to generate the flame, the nozzle locates in the center, the diameter of the nozzle is 12 *mm*. The flow rate of fuel ethylene is 300 *ml*/*min*, and the surrounding airflow rate is 10 *L*/*min*. Such a structure is known as the co-flow burner. The second experiment is conducted to verify the reconstruction accuracy of LFSP under a complex flame structure. To achieve that, a double-peak flame is generated because the flame structure can be pre-known from the designed burner, which is useful in verification. A nozzle plate with two fuel nozzles is used to generate the double-peak flame, the diameters of the nozzles are 8 *mm*, the distance between the center of nozzles is 25 *mm*. The ethylene flow rates in both nozzles are 50 *ml*/*min*, and the airflow rate is 5 *L*/*min.* The last experiment is used to demonstrate that the LFSP can measure the local temperature distribution of instantaneous turbulent flames. This capability is of importance for LFSP because turbulent flames widely exist in various combustion applications. In this experiment, a periodic pulsating flame is generated using a nozzle plate with three fuel nozzles. Those three nozzles are arranged as a triangle, and the distances between the center of each nozzle are 25 *mm*.

This structure refers to the application of multi-burner combustion, such as diesel engine injectors or gas turbine combustors [5]. The flow rates of fuel ethylene for each nozzle are 500 ml/min, and the airflow rate is 5 L/min. The detailed description of these experiments and the evaluation of LFSP are discussed as follows.

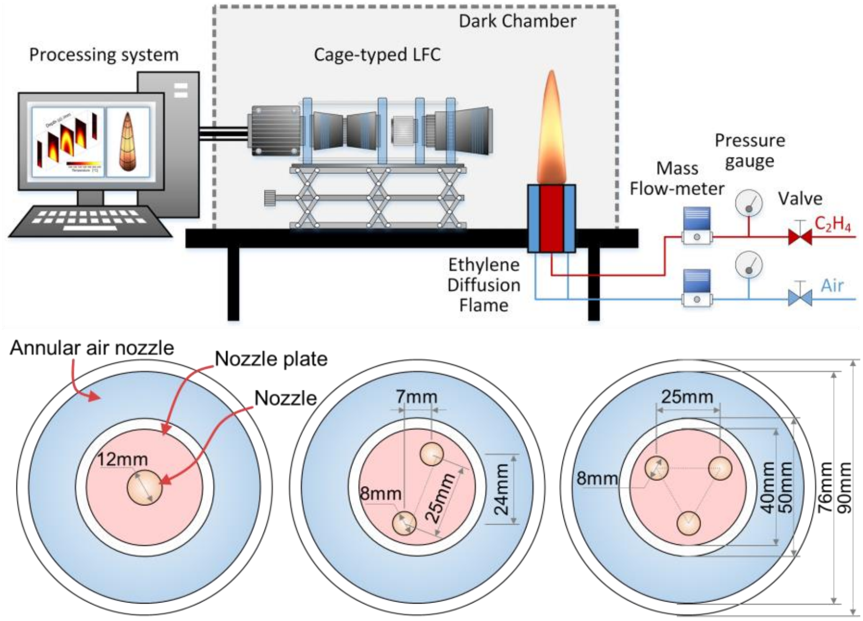

Fig. 14. The schematic of the experiment setup and the structure of three different burner plates.

6.2 Evaluation of LFSP through a laminar diffusion flame

To evaluate the reconstruction accuracy of flame temperature through the LFSP, a stable flame segment with a significant temperature gradient is desired. A co-flow burner is used to generate a laminar ethylene-air diffusion flame, as shown in Fig. 15(a). Studies [1–3,11] suggested that the lower part of the ethylene diffusion flame through a co-flow burner generates the highest temperature gradient and keeps laminar. Therefore, the measuring height of the flame area is set at 45 mm in this experiment. Fig. 15(a) shows the marked area (red frame) of the measuring height, where the flame diameter is approximately 8 mm. The reconstructed intensity distribution of the flame sections is shown in Fig. 15(b). The temperature distribution of the flame section at depth $z = 0\,mm$ was solved using the CRP, as shown in Fig. 15(c). The flame temperature is higher at the edge (x-axis direction) but relatively low in the center. The histogram of the pixel temperature distribution of the flame section ($z = 0\,mm$) is shown in Fig. 15(d), which illustrates that the flame temperature is mainly distributed at the range of 1100~1400°C. Similar trends were reported in the Refs. [1–3,11,44].

The reconstructed temperature is compared with thermocouple measurements to evaluate the temperature measurement quantitatively. An R-type thermocouple (wire diameter is 0.51 mm) is used to measure the flame temperature along the x-axis with an interval of 1.4 mm while $y = 47.5 \pm 1\,mm$ and $z = 0\,mm$. For each position, 50 temperature readings were taken with the reading rate of one read/sec. The temperature read-out starts after the thermocouple is inserted into the flame, and the junction is covered by soot (approximately five seconds) [1]. The read-out temperatures are then used to estimate the flame temperature based on the heat transfer balance between the convective and radiative heat transfer of the thermocouple [8,45]. The estimated flame temperatures are plotted in Fig. 15(e). Each point is the mean flame temperature corresponding to the 50 thermocouple readings, and the error bar is two times the standard deviation. The temperature calculated using LFSP is also shown in Fig. 15(e). It is shown that the temperature distributions of the two measurements are in good agreement, where the local highest temperature appears at both ends, and the temperature in the center of the flame is slightly lower. These results demonstrate that the flame temperature measurement of LFSP is reliable.

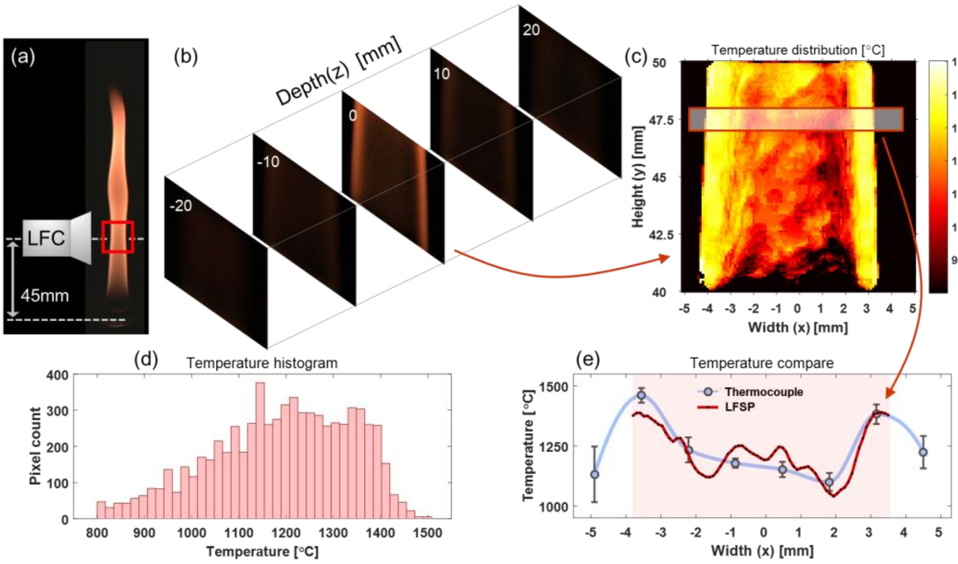

Fig. 15. The measuring area of an ethylene flame (a), the reconstructed sectional radiation distribution of the flame (b), the flame temperature distribution of the center section at $z = 0\ mm$ (c), the pixel temperature histogram of the center section (d), and the comparison of flame temperature between the LFSP and thermocouple measurement at $y = 47.5 \pm 1\ mm$ and $z = 0\ mm$ (e) where the thermocouple measurement is corrected, the errorbar is two times of standard deviation. Note that Fig. (b) is not scaled.

Note that the LFSP result is fluctuating along the x-axis, but the thermocouple results are relatively smooth. However, it is not comparable directly between the temperature of thermocouple and LFSP because their spatial and temporal scales are different. The welding junction bead of the thermocouple wires has a non-negligible diameter (>1 *mm*) and thermal inertia, which means each thermocouple measurement is fundamentally an integration of the temperature in a range of space and time. Therefore, the thermocouple temperature result is smooth and cannot reflect spatial details or the instantaneous temperature change of a flame. On the contrary, the LFSP has a high lateral and temporal resolution, so the temperature measurement of LFSP can reflect fine spatial details, as well as the temperature distribution at a specific moment. Fig. 15(e) shows that the LFSP retrieve 71 data points along the width direction (x-axis), so the lateral resolution provided by LFSP is about 0.11 *mm*, which is consistent with the theoretical lateral resolution listed in Table 1.

6.3 Evaluation of LFSP through a double-peak flame

To verify the capability of LFSP to reconstruct complex flame temperature, an experiment was carried out to reconstruct the double-peak flame. Fig. 16(a) shows the experimental setup of the double-peak flame. Two LF refocus images were focused on the front and the rear of the flame, as shown in Fig. 16(b). In the LF refocus images, the flame on the left is closer to the LFC. The depth distance between the two flames is 24 *mm* along the z-axis direction. Five sections were reconstructed with an interval of 12 *mm*, which is considered based on the depth resolution mentioned in Table 1 and Section 4.3. The sectional radiation intensity distributions with different depths are shown in Fig. 16(c).

Ideally, the flame structure should be reconstructed only on the depth of +12 *mm* and -12 *mm*, since there is no flame existing on the other depth positions (i.e., +24 *mm*, 0 *mm*, and -24 *mm*). In Fig. 16(c), the flame sections corresponding to the locations +12 *mm* and -12 *mm* have significant differences in radiation intensity distribution, and they are closely matched with the position and shape of the actual flames. It can be seen that the intensity contribution of the defocused flame sections is completely removed from both flame sections (12 *mm* and -12 *mm*) compared to the LF refocus images. Even though the two flames are partially overlapped in the LF refocus images, the boundary of the flame can be retrieved clearly and continuously. This phenomenon shows that the overlapping of the flames does not affect the reconstruction result. These results indicate that the LFSP can reconstruct the flames at different depths accurately when the intervals of flame sections matched with the depth resolution as solved in Section 4.3.

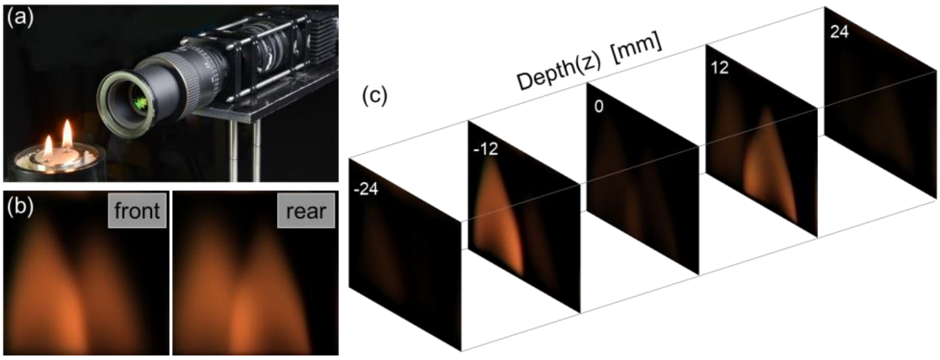

Fig. 16. The experiment setup of the double-flame (a), the LF refocus images focusing on each flame, respectively (b), the reconstructed sectional radiation distribution with different depth positions.

6.4 Reconstruction of turbulent flame temperature

The proposed LFSP is further verified to reconstruct the instantaneous temperature of a turbulent flame. The periodic pulsating phenomena of the turbulent flame is recorded using a high-speed camera at 240 *fps*, as shown in Fig. 17(a). The period of each flame pulsation is approximately 167 *ms* (the frequency is ~6.0 *Hz*). In each pulsating period, a flaming fireball is generated in the beginning, after emitting bright yellow radiation, the fireball extinguishes and finally emits a large number of soot particles upward. The fireball is formed about 110 *mm* height from the burner exits. The fireball diameter is up to 90 *mm* by analyzing the flame image in Fig. 17(a). The internal structure of the fireball is complex and changing suddenly with time, which poses a challenge for flame reconstruction.

The cage-typed LFC is positioned to capture the flame at the height of 110 mm, where the flame fireball is located. The camera exposure time is set to 1.0 *ms* to ensure that the flame is not too bright or too dark. The field of view of the cage-typed LFC is marked using the red dash line in Fig. 17(a). An example of the LF view-shift images of the flame is shown in Fig. 17(b). The moment when those LF view-shift images were captured is estimated between 63 *ms* and 83 *ms*, referring to Fig. 17(a). In Fig. 17(b), it is observed that there is no significant movement of the upper left and lower right corners of the flame compared with the left and right views of the flame. In the meantime, the other two flame outlines (marked using white dash lines in the center area) moved in the opposite direction. The movement indicates that there are at least three flames located in different depths. According to Fig. 10, it can be explained that the flame in the upper left and lower right corners should be located on the object plane of the LFC, and the other two flame structures in the center are probably located on the near side and rear sides of the object plane, respectively. This can be verified by reconstructing the flame radiation intensity distribution at different depths. Fig. 17(c) shows the reconstructed flame radiation intensity distribution at different depths where the sharpest flame structures are marked using white dash lines. It is suggested that the flames at the two corners are sharp in the object plane ($z = 0\ mm$). Another two flame structures are clearly shown in the depth of $z = -10\ mm$ and $z = +10\ mm$, respectively. This result is consistent with the explanation derived from the flame images in Fig. 17(b). Such an agreement indicates that the LFSP can penetrate the flame and reconstruct the radiation intensity at different depths accurately.

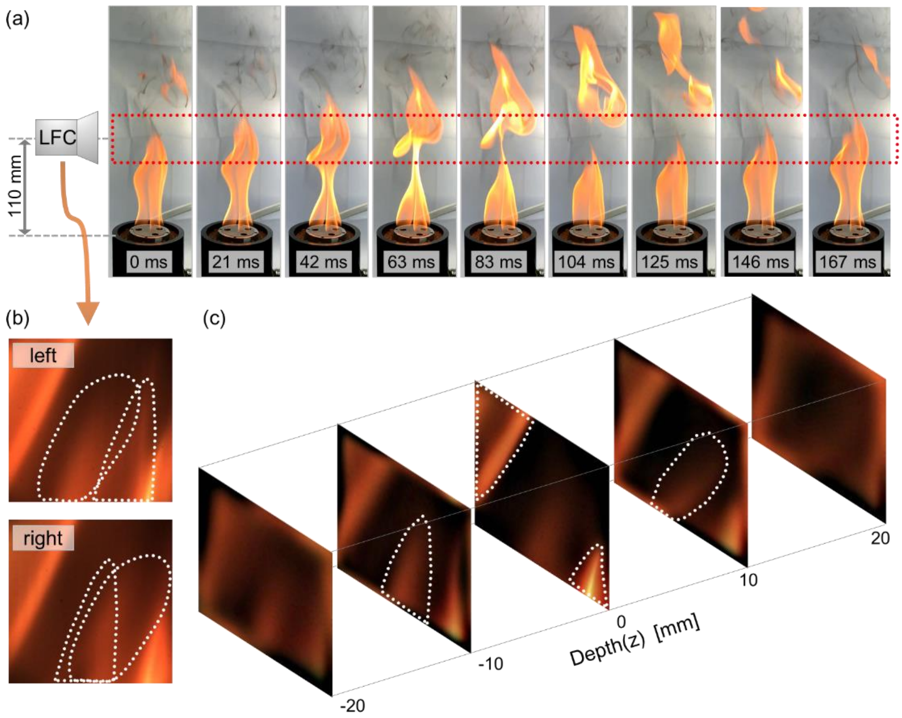

Fig. 17. (a) The periodic pulsation of a turbulent ethylene flame with a planar light source in the background captured by a high-speed camera at 240 *fps* (see **Video 3**), (b) an example of LF view-shift images of the flame (see **Video 4**), (c)the reconstructed radiation intensity distribution at different depths.

Once the flame radiation intensity is reconstructed at different depths, the flame temperature is then calculated, as shown in Fig. 18. It can be seen that the flame has a wide temperature distribution, ranging from 600 °C to 1800 °C. The highest temperature is in the lower right corner. The black area is cut off and set to none as the calculated temperature below 600 °C. While comparing the flame temperature distributions in different depths (Fig. 18), it is found that the temperature change of flame is continuous along the depths. As can be seen from Fig. 18(a) to Fig. 18(d), the flame in the center is surrounded by another flame in the periphery, where the gap between two flame structures is up to 2 *mm*. It is also observed that the temperature of the center flame is lower than that of the outer flame. This phenomenon indicates that the fireball probably has a multi-layer structure, and there is a temperature gradient that the outside layer of the flame is of higher temperature.

Additionally, some vortex-like structures of the flame temperature are observed in Fig. 18(a), Fig. 18(d), and Fig. 18(e). Those vortex-like temperature distributions suggest that there are vortex flows during the flame pulsation, possibly this is the reason for the relatively low temperature of the center area. Considering that the fast flow will decrease the residence time of the fuel, together with the observed local low temperature, such a phenomenon may lead to incomplete combustion and result in soot formation [5,44,46]. These observations demonstrate the LFSP can reconstruct the instantaneous temperature distribution of a turbulent flame with a high spatial resolution. Thus, the LFSP can widely be applied to the academic or industrial applications to measure the turbulent sooting flames temperature.

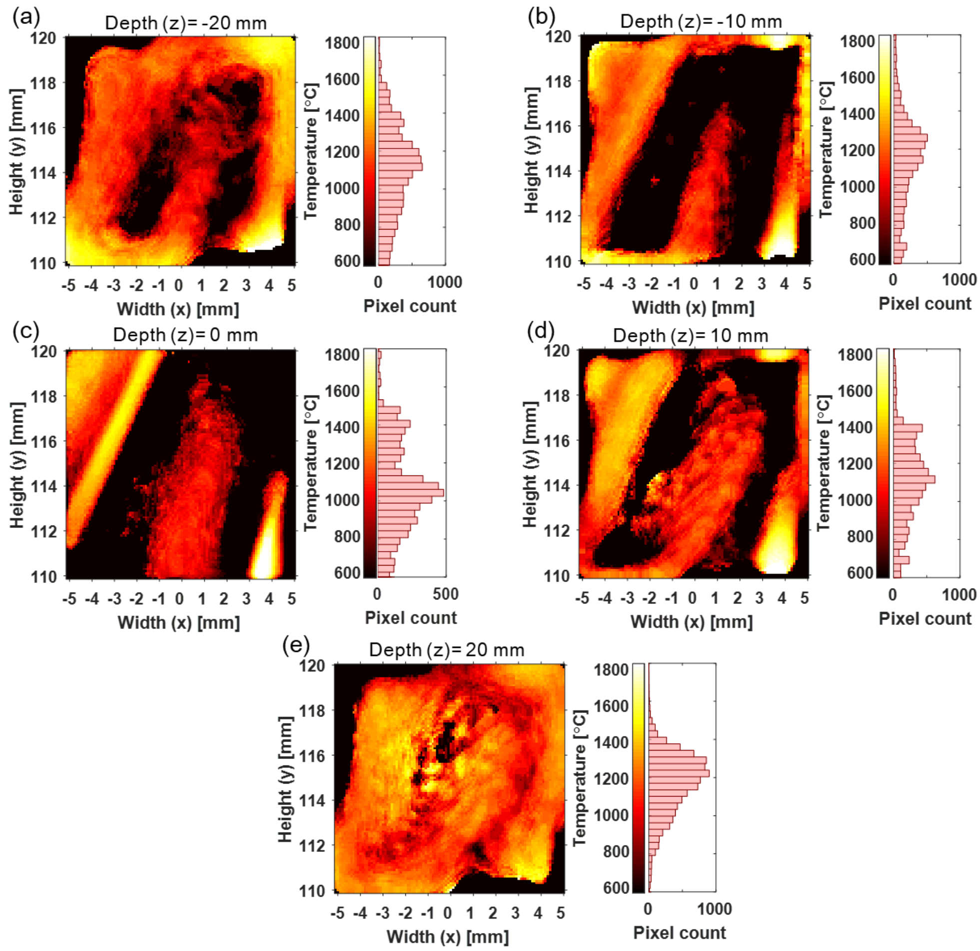

Fig. 18. The flame temperature distribution at different depths. The black area is cut off, where the temperature is below 600°C.

7. Conclusion

In this study, the spatial resolution of the light field sectioning pyrometry (LFSP) technique is evaluated for flame temperature measurement. The algorithm of LFSP is introduced. A theoretical model of the spatial resolution is proposed based on optical parameters and point spread function of the light field camera (LFC). The spatial resolution (i.e., the depth resolution and lateral resolution) of LFSP for different LFCs along with the proposed cage-typed LFC are analyzed through numerical simulation. The quantitative difference between the depth and lateral resolution was discussed. The proof-concept of the proposed cage-typed LFC is evaluated through different experiments. The temperature distributions of both laminar and turbulent diffusion flames are reconstructed using the LFSP at different depths of the flame. The concluding remarks obtained from this study are summarized as follows:

- It has been observed that the depth resolution depends on the LFC parameters (i.e., the focal length of the main lens, the object distance, the aperture diameter of the main lens). Thus, the depth resolution can further be improved by utilizing optimize LFC parameters.
- For different LFCs, a better lateral resolution is achieved compared to the depth resolution, and the quantitative difference is 100 times larger. Such a difference was fundamentally determined by the characteristics of the light field imaging and the LFSP algorithm.
- The comparative study suggested that the proposed cage-typed LFC can provide an excellent spatial resolution compared to the existent LFCs. The lateral and depth resolution of the cage-typed LFC are 100 μm and 10.5 mm, respectively, which are 17% and 50% improved compared to the typical LFC.

This work demonstrates that the LFSP can retrieve the 3-D temperature field with a high spatial resolution for turbulent flames compared to the other light-field pyrometry techniques. The LFSP has advantages of simplicity of apparatus and fast response, which can be used to monitor flames for various purposes, such as fundamental combustion research and industrial applications.

Acknowledgement

This work was supported by the National Natural Science Foundation of China (51976038); the Fundamental Research Funds for the Central Universities (2242019k1G018); and the Fund of the State Key Laboratory of Technologies in Space Cryogenic Propellants (SKLTSCP1908). The authors also thank the editors and referees who made important comments that helped us improve this paper.

Reference

1. C. S. McEnally, Ü. Ö. Köylü, L. D. Pfefferle, and D. E. Rosner, "Soot volume fraction and temperature measurements in laminar nonpremixed flames using thermocouples," Combust. Flame **109**, 701–720 (1997).
2. P. B. Kuhn, B. Ma, B. C. Connelly, M. D. Smooke, and M. B. Long, "Soot and thin-filament pyrometry using a color digital camera," Proc. Combust. Inst. **33**, 743–750 (2011).
3. H. Liu, S. Zheng, and H. Zhou, "Measurement of Soot Temperature and Volume Fraction of Axisymmetric Ethylene Laminar Flames Using Hyperspectral Tomography," IEEE Trans. Instrum. Meas. **66**(2), 315–324 (2017).
4. Y. Yan, T. Qiu, G. Lu, M. M. Hossain, G. Gilabert, and S. Liu, "Recent advances in flame tomography," Chinese J. Chem. Eng. **20**(2), 389–399 (2012).
5. T. Xuan, J. M. Desantes, J. V. Pastor, and J. M. Garcia-Oliver, "Soot temperature characterization of spray a flames by combined extinction and radiation methodology," Combust. Flame **204**, 290–303 (2019).
6. K. Srinivasan, T. Sundararajan, S. Narayanan, T. J. S. Jothi, and C. S. L. V. Rohit Sarma, "Acoustic pyrometry in flames," Measurement **46**, 315–323 (2013).
7. G. Liu and D. Liu, "Inverse radiation analysis for simultaneous reconstruction of temperature and volume fraction fields of soot and metal-oxide nanoparticles in a nanofluid fuel sooting flame," Int. J. Heat Mass Transf. **118**, 1080–1089 (2018).
8. M. M. Hossain, G. Lu, D. Sun, and Y. Yan, "Three-dimensional reconstruction of flame temperature and emissivity distribution using optical tomographic and two-colour pyrometric techniques," Meas. Sci. Technol. **24**(7), 13–17 (2013).
9. M. M. Hossain, G. Lu, and Y. Yan, "Optical fiber imaging based tomographic reconstruction of burner flames," IEEE Trans. Instrum. Meas. **61**(5), 1417–1425 (2012).
10. K. Wang, F. Li, H. Zeng, and X. Yu, "Three-dimensional flame measurements with large field angle," Opt. Express **25**(18), 21008–21018 (2017).
11. C. Xu, W. Zhao, J. Hu, B. Zhang, and S. Wang, "Liquid lens-based optical sectioning tomography for three-dimensional flame temperature measurement," Fuel **196**, 550–563 (2017).
12. H. Ren and S.-T. Wu, "Variable-focus liquid lens," Opt. Express **15**(10), 5931–5936 (2007).
13. R. Ng, M. Levoy, M. Bredif, G. Duval, M. Horowitz, and P. Hanrahan, "Light Field Photography with a Hand-held Plenoptic Camera," in *Stanford Tech Report CTSR* (2005), pp. 1–11.
14. W. Zhao, B. Zhang, C. Xu, L. Duan, and S. Wang, "Optical sectioning tomographic reconstruction of three-dimensional flame temperature distribution using single light field camera," IEEE Sens. J. **18**(2), 528–539 (2018).
15. T. Li, Y. Yuan, Y. Shuai, and H. Tan, "Joint method for reconstructing three-dimensional temperature of flame using Lucy-Richardson and nearest neighbor filtering using light-field imaging," Sci. China Technol. Sci. **62**(7), 1232–1243 (2019).
16. T. Georgiev, K. C. Zheng, B. Curless, D. Salesin, S. Nayar, and C. Intwala, "Spatio-angular resolution tradeoffs in integral photography," in *Eurographics Symposium on Rendering* (2006), pp. 263–272.
17. J. Sun, C. Xu, B. Zhang, M. M. Hossain, S. Wang, H. Qi, and H. Tan, "Three-dimensional temperature field measurement of flame using a single light field camera," Opt. Express **24**(2), 1118–1132 (2016).
18. Y. Liu, M. M. Hossain, J. Sun, B. Zhang, and C. Xu, "Investigation and optimization of sampling characteristics of light field camera for flame temperature measurement," Chinese Phys. B **28**(3), 034207 (2019).
19. V. Drazic, "Optimal depth resolution in plenoptic imaging," in *IEEE International Conference on Multimedia and Expo* (IEEE, 2010), pp. 1588–1593.
20. E. A. Deem, Y. Zhang, L. N. Cattafesta, T. W. Fahringer, and B. S. Thurow, "On the resolution of plenoptic PIV," Meas. Sci. Technol. **27**(8), 084003 (2016).
21. S. Zhu, A. Lai, K. Eaton, P. Jin, and L. Gao, "On the fundamental comparison between unfocused and focused light field cameras," Appl. Opt. **57**(1), 1–11 (2018).
22. X. Song, M. Gu, L. Cao, Z. Tang, and C. Xu, "A microparticle image velocimetry based on light field imaging," IEEE Sens. J.

19(21), 9806–9817 (2019).

23. D. G. Dansereau, O. Pizarro, and S. B. Williams, "Decoding, calibration and rectification for lenselet-based plenoptic cameras," in *Proceedings of the IEEE Computer Society Conference on Computer Vision and Pattern Recognition* (2013), pp. 1027–1034.
24. R. Ng, "Fourier slice photography," ACM Trans. Graph. **24**(3), 735–744 (2005).
25. D. G. Dansereau, O. Pizarro, and S. B. Williams, "Linear Volumetric Focus for Light Field Cameras," ACM Trans. Graph **53**(9), 1689–1699 (2013).
26. E. Hecht, *Optics*, 5th ed. (Pearson, 2017).
27. P. Sarder and A. Nehorai, "Deconvolution methods for 3-D fluorescence microscopy images," IEEE Signal Process. Mag. **23**(3), 32–45 (2006).
28. J. L. Urban, M. Vicariotto, D. Dunn-Rankin, and A. C. Fernandez-Pello, "Temperature Measurement of Glowing Embers with Color Pyrometry," Fire Technol. **55**(3), 1013–1026 (2019).
29. Y. Liu, J. L. Urban, C. Xu, and C. Fernandez-Pello, "Temperature and Motion Tracking of Metal Spark Sprays," Fire Technol. **55**(6), 2143–2169 (2019).
30. V. N. Mahajan, "Uniform versus Gaussian beams: a comparison of the effects of diffraction, obscuration, and aberrations," J. Opt. Soc. Am. A **3**(4), 470–485 (1986).
31. C. Guo, W. Liu, X. Hua, H. Li, and S. Jia, "Fourier light-field microscopy," Opt. Express **27**(18), 25573–25594 (2019).
32. D. F. Swinehart, "The Beer-Lambert law," J. Chem. Educ. **39**(7), 333–335 (1962).
33. T. Li, S. Li, Y. Yuan, F. Wang, and H. Tan, "Light field imaging analysis of flame radiative properties based on Monte Carlo method," Int. J. Heat Mass Transf. **119**, 303–311 (2018).
34. J. D. Felske and C. L. Tien, "Calculation of the Emissivity of Luminous Flames," Combust. Sci. Technol. **7**(1), 25–31 (1973).
35. T. Li, S. Li, S. Li, Y. Yuan, and H. Tan, "Correction model for microlens array assembly error in light field camera," Opt. Express **24**(21), 24524–24543 (2016).
36. Z. Wang, A. C. Bovik, H. R. Sheikh, and E. P. Simoncelli, "Image quality assessment: From error visibility to structural similarity," IEEE Trans. Image Process. **13**(4), 600–612 (2004).
37. T. Georgiev, Z. Yu, A. Lumsdaine, and S. Goma, "Lytro camera technology: theory, algorithms, performance analysis," in *Multimedia Content and Mobile Devices* (2013), **8667**, pp. 1–10.
38. A. Fischer, C. Kupsch, J. Gürtler, and J. Czarske, "High-speed light field camera and frequency division multiplexing for fast multi-plane velocity measurements," Opt. Express **23**(19), 24910–24922 (2015).
39. K. He, X. Wang, Z. W. Wang, H. Yi, N. F. Scherer, A. K. Katsaggelos, and O. Cossairt, "Snapshot multifocal light field microscopy," Opt. Express **28**(8), 12108–12120 (2020).
40. Z. P. Tan, R. Alarcon, J. Allen, B. S. Thurow, and A. Moss, "Development of a high-speed plenoptic imaging system and its application to marine biology PIV," Meas. Sci. Technol. **31**, 1–11 (2020).
41. T. Li, S. Li, Y. Yuan, Y. Liu, C. Xu, Y. Shuai, and H. Tan, "Multi-focused microlens array optimization and light field imaging study based on Monte Carlo method," **25**(7), 8274–8287 (2017).
42. S. Brisken and M. Martella, "Multistatic ISAR autofocus with an image entropy-based technique," IEEE Aerosp. Electron. Syst. Mag. **29**(7), 30–36 (2014).
43. K. Masaoka, T. Yamashita, Y. Nishida, and M. Sugawara, "Modified slanted-edge method and multidirectional modulation transfer function estimation," Opt. Express **22**(5), 6040–6046 (2014).
44. R. J. Santoro and T. F. Richardson, "Concentration and temperature effects on soot formation in diffusion flames," in *Soot Formation in Combustion*, H. Bockhom, ed. (Springer-Verlag, 1994), pp. 221–238.
45. V. Hindasageri, R. P. Vedula, and S. V. Prabhu, "Thermocouple error correction for measuring the flame temperature with determination of emissivity and heat transfer coefficient," Rev. Sci. Instrum. **84**(2), 024902 (2013).
46. D. S. Bento, K. A. Thomson, and Ö. L. Gülder, "Soot formation and temperature field structure in laminar propane-air diffusion flames at elevated pressures," Combust. Flame **145**(4), 765–778 (2006).